Surface Wave and Roller Dissipation Observed with Shore-based Doppler Marine Radar

Michael Streßer[1], Jochen Horstmann[1], and Burkard Baschek[1*]

[1]Helmholtz-Zentrum Hereon, Max-Planck-Straße 1, 21502 Geesthacht, Germany

Key Points:

- high-resolution observations of surface wave and roller dissipation as well as the transformation of wave height across the surf zone
- the concept of surface rollers is applied to shore-based X-band Doppler radar data
- in storm conditions, 50% of the wave energy is dissipated at a submerged outer sandbar, but strongest dissipation occurs further inshore

*current affiliation: Deutsches Meeresmuseum, Katharinenberg 14 - 20, 18439 Stralsund, Germany

Corresponding author: Michael Streßer, michael.stresser@hereon.de

Abstract

Surface wave energy and dissipation are observed across the surf zone. Utilizing the concept of surface rollers, a new scaling is introduced to obtain the energy flux and dissipation related to rollers from Doppler velocities measured by a shore-based X-band marine radar. The dissipation of wave energy and hence the transformation of the incoming wave height (or energy) is derived using the coupled wave and roller energy balance equations. Results are compared to in-situ wave measurements obtained from a wave rider buoy and two bottom mounted pressure wave gauges. A good performance in reproducing the significant wave height is found yielding an overall root-mean-square error of 0.23 m and a bias of -0.13 m. This is comparable to the skill of numerical wave models. In contrast to wave models, however, the radar observations neither require knowledge of the bathymetry nor the incident wave height. Along a 1.5 km long cross-shore transect on a double-barred, sandy beach in the southern North Sea, the highest dissipation rates are observed at the inner bar over a relatively short distance of less than 100 m. During the peak of a medium-severe storm event with significant wave heights over 3 m, about 50% of the incident wave energy flux is dissipated at the outer bar.

Plain Language Summary

Ocean waves are carrying a large amount of mechanical energy which they have gained from the wind blowing over the ocean surface. At the coast this energy supply generates strong water motions, creates forces on coastal structures, moves sand, and can cause coastal erosion. It is therefore important to know when, where, and to what extent wave energy is reduced under different environmental conditions. The majority of the energy is removed by wave breaking. However, this process is still not completely understood which is partly due to fact that it is difficult to observe. This is particularly the case during storm conditions when it is very complicated to install and recover measurement equipment in the ocean. The present work describes a methodology to obtain such measurements using a special radar device which is installed at the beach; hence, it is not being impacted by harsh wave conditions. This approach will enable scientists to perform long-term monitoring of wave breaking thus opening new opportunities to study beach processes and coastal changes.

1 Introduction

The Earth's coastlines are facing sea level rise and increased human interventions. Predicting long-term coastal changes is of major importance to ensure efficient planning and design of coastal structures as well as a sustainable management of the coastal zone. Furthermore, a proper incorporation of nearshore processes into earth system models is required to efficiently predict the future changes of the coastal morphology, i.e. coastal morphodynamics. Long-term measurements of nearshore hydrodynamics, in particular the spatial distribution of wave heights, are rarely available but often required to develop, validate, or calibrate parameterizations of nearshore processes.

In the surf zone, breaking surface waves are the main drivers of hydro- and morphodynamics. When waves break, energy is removed from the wave field and transferred to turbulence, currents, sound and heat. Therefore, wave breaking and associated wave energy dissipation link the wave energy flux to surf zone mixing and sediment transport. A "direct measurement of wave dissipation is equivalent to measuring the forcing for nearshore flow" (Holman & Haller, 2013). However, deployment and maintenance of in-situ sensors, e.g. wave staffs, acoustic sensors or pressure transducers, is difficult in particular within energetic breaking wave conditions. Moreover, large arrays of synchronized in-situ sensors are needed to capture the high spatial and temporal variability of the nearshore wave field.

This has motivated the development of close-range remote sensing techniques, that come with the benefit of providing continuous data at high resolution in space and time. Space-time measurements of the surface elevation can be obtained by scanning lidar (Martins et al., 2016, 2018) or stereo photogrammetry (Bergamasco et al., 2017). However, both methods can cover only a very limited distance (around 100 m) thus preventing applications over wide surf zones if no infrastructure, like a peer, is available. Coastal video monitoring systems typically provide better ground coverage and can be used to derive local bathymetry (Holman et al., 2013; Aarninkhof et al., 2005), currents (Chickadel et al., 2003), or both in combination (Dugan et al., 2001). In contrast to passive camera sensors, imaging marine radar is an active remote sensing technique. As such, it can be operated during day and night as well as in bad (foggy) view conditions. It provides larger spatial coverage and much easier geo-referencing. Incoherent marine radar can be used to infer currents (Senet et al., 2001; Lund et al., 2018, among others) and bathymetry (Senet et al., 2008; Bell & Osler, 2011; Lund et al., 2018; Chernyshov et al., 2020, among others) as well as directional wave spectra (Nieto Borge et al., 1999). Radar-based techniques to retrieve wind, currents and bathymetry were reviewed by Horstmann et al. (2015). Huang et al. (2017) focused on wind and wave retrievals from radar. Radar-based retrieval of currents from wave dispersion outside the surf zone has been shown to provide a remarkable accuracy with a root-mean-square error (RMSE) below 0.04 m/s.

The retrieval of the wave height and hence wave energy using remote sensing is more difficult, in particular for spatially varying wave fields. McGregor et al. (1998) were able to estimate local wave energy and water depths before and after a sandbar using imaging (S-band) Doppler radar. Their radar system, however, was located on a cliff 70 m above the water surface; thus, grazing angles were still relatively high ($> 8°$). Under such moderate incidence angles, radar backscatter is relatively well understood and Bragg scattering is the dominating scattering mechanism (e.g. Valenzuela, 1978). Therefore, the Doppler velocity measured by the radar can be transformed to sea surface elevation through wave theory (e.g. Plant et al., 1983). At low grazing angles, the backscatter modulation mechanisms change and other (mostly nonlinear) scattering mechanisms, e.g. small-scale wave breaking or wedge scattering, become important (for details refer to the special issue by Brown, 1998). This hinders a direct inversion of the radar signal to surface elevation. For incoherent radars, the non-linearities resulting from the imaging are traditionally eliminated through the application of a bandpass filter around the linear wave dispersion relation in the wavenumber-frequency domain in combination with an empirical modulation transfer function (MTF, Nieto Borge et al., 1999, 2004). This requires intensive calibration for every individual radar installation. In the nearshore, however, waves, currents, and the bathymetry vary on short distances. Therefore, the homogeneity assumption is violated and it is often not possible to apply a properly defined dispersion filter. In homogeneous conditions, a calibration-free measurement of the significant waves height is possible using Doppler radar (Carrasco et al., 2017), but the need for dispersion filtering remains. Recently, Navarro et al. (2019) presented a promising, potentially calibration-free, approach to estimate the significant wave height from incoherent radar and applied it to study wave heights on a coral reef (Navarro et al., 2021).

Another approach that has been used in nearshore remote-sensing is to estimate wave dissipation instead of trying to measure the wave height. Wave dissipation indicates a loss of wave energy and is directly influencing many surf zone processes such as turbulence production or wave-induced currents. A proxy for wave dissipation is the presence of surface rollers, i.e. the turbulent air-water mixture sliding down the front faces of breaking waves. The geometrical properties of the roller can be used to estimate dissipation (Duncan, 1981). Figure 1 shows a sketch of a breaking wave carrying a surface roller. The roller concept has been applied to time-avaraged video (Aarninkhof & Ruessink, 2004), or more recently to thermal images (Carini et al., 2015), a combination of visible video and radar (Flores et al., 2016; Díaz et al., 2018), as well as scanning lidar data (Martins et al., 2018).

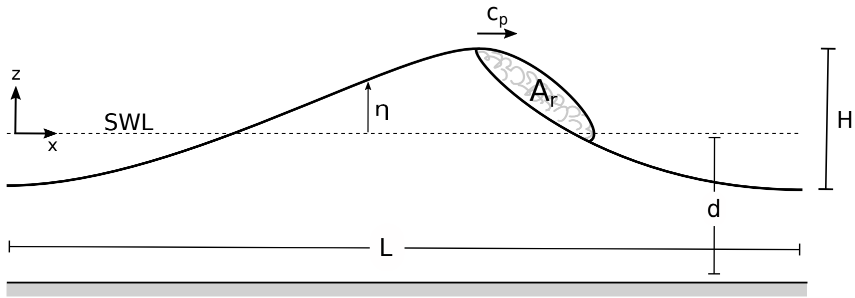

Figure 1. Illustration of the cross-section of a breaking wave carrying a surface roller with cross-sectional area A_r. Shown is the local surface elevation η, i.e the location of the free surface with respect to still water level (SWL). H is the wave height measured from crest-to-trough, L and d are wave length and mean water depth. The wave crest moves at the wave phase speed c_p in the positive x-direction.

Within the present paper, we propose a new approach to apply the roller concept to Doppler radar data recorded by a shore-based, coherent-on-receive X-band marine radar. Preliminary results of this work were presented by Streßer and Horstmann (2019). Unlike camera based methods, which estimate dissipation based on geometrical roller properties, the proposed method is based on roller kinematics. More specifically the increase from slow to fast surface speeds at the toe (the front edge) of the surface roller is related to roller energy and dissipation. It can be obtained from the Doppler velocity measured by the radar. The method is used to efficiently obtain mean dissipation rates with high spatial resolution (7.5 m) along a cross-shore transect spanning the entire surf zone (> 1 km) of a double-barred, sandy beach.

The paper is structured as follows: The field measurements are described in section 2. In section 3, the scaling to obtain dissipation is first derived empirically through a comparison to the in-situ observations and then theoretically from physical principles. The evolution of radar-derived roller dissipation during a 3-day storm event is shown in section 4. In section 5, the cross-shore transformation of the wave height is presented and the performance of the method is studied by comparing it to in-situ measurements and simulations. Section 6 contains an investigation of the wave energy flux budget with an attribution of the observed dissipation to the morphological features. The transferability of the results to other sites as well as the expected uncertainty are discussed in section 7 and, finally, a conclusive summary is given in section 8.

2 Field Observations at Bunkerhill Beach, Sylt

The field measurements used for the present study were conducted from Sep 27 to Oct 1, 2016. The study area is located at Bunkerhill beach on the German North Sea island Sylt. Sylt is located close to the border between Germany and Denmark, and is the northernmost of the German barrier islands separating the Southern North sea from the intertidal flats of the Wadden Sea. The measurements where obtained at the West coast of the island in front of a long-term radar station operated by the Helmholtz-Zentrum Hereon. The beach can be classified as sandy, submesotidal, mixed-energy beach (equally influenced by tidal currents and wave action) with a median grain size of $D_{50} = 0.55$ mm (LKN.SH, 2015).

At the study site, the coastline is oriented at a small inclination of 2° with respect to North. The local coordinate reference system used in this paper has the origin at the location of the radar station (54.7903° N, 8.2833° E). The x- and y-axis are pointing towards East and North, respectively. The beach topography at the study site is shown in fig. 2. The subtidal region is composed of tide-corrected and quality-checked bathymetric data constructed from single-beam echo soundings recorded between Sep 22 - 26, 2016 (Cysewski et al., 2019). For the shown 2 km long stretch of the coastline, the subtidal bathymetry is uniform in the alongshore direction. The intertidal area and the dry beach are covered by airborne lidar data acquired on Sep 26, 2016, by the state of Schleswig-Holstein's Government-Owned Company for Coastal Protection, National Parks and Ocean Protection (LKN.SH). The data are mapped to a 5 m x 5 m grid along the cross-shore transect in front of the radar station by averaging all data points within one grid cell. The cross-shore beach profile shows a subtidal sandbar with the crest located at $x = -500$ m at a vertical elevation $z \approx -4.5$ m-MSL, and an intertidal bar at $x = -160$ m and $z \approx -0.5$ m-MSL. The shoreline at a normal high water is at $x \approx -100$ m.

The incident wave field is available from a wave rider buoy (a Datawell DWR-MkIII) located at $x = -1100$ m. Two bottom mounted pressure transducers (Measurement Specialties 86BSD-050PA) were deployed in the intertidal region to provide wave height measurements at the inner bar. The first pressure gauge (PG_A) was located at the trough of the inner bar at $x = -127.5$ m and provided data until Sep 30. The second (PG_B) provided data for the entire study period and was located at $x = -180$ m, which is $\approx$ 30 m offshore of the bar crest. The pressure signal was logged at 10 Hz and transformed to surface elevation using the weakly non-linear method of Bonneton et al. (2018). On recovery, the pressures gauges were immersed into the sand by ≈ 30 cm yielding an the expected error < 3 % considering an exponential damping due to burial (Raubenheimer et al., 1998). Water elevation and currents due to the tide and surge, as well as the 10-m wind speed are available from the operational model BSHcmod (Dick, 2001) operated by the "Bundesamt für Seeschiffahrt und Hydrographie" (BSH), the German federal hydrographic and maritime traffic agency. Deviations from the true surface elevation during the bathymetry measurements were below 0.15 m, indicating a reasonable accuracy of the operational model for the purpose of the present study.

The sea state is mostly locally generated and grows rapidly from 0.5 m to ≈ 2 m significant wave height on the second half of Sep 27. Simultaneously, the peak wave period increases from 4 s to around 8 s. While wave periods remain constant around 8 s on Sep 28, they increase further on Sep 29 reaching a maximum of 10.5 s on Sep 30, 01:00 UTC. The maximum significant wave height of 3.3 m is reached a little earlier, on Sep 29, 23:00 UTC, and remained constant on this level for 3 hours. Afterwards, the significant wave height decreases rapidly to 2 m on Sep 30, 03:00 UTC. During the following 24 hours it drops further to a level of about 1 m on Oct 1, 03:00 UTC. Throughout the entire storm, wind speeds and significant wave heights are highly correlated indicating a young, locally generated sea state. Both, waves and winds during the storm were directed onshore, approaching from West, i.e 270°.

2.1 Coherent X-band Radar Measurements

2.1.1 Radar hardware

The radar used in this study is a coherent-on-receive marine radar developed at the Helmholtz-Zentrum Hereon (Hereon, formerly Helmholtz-Zentrum Geethacht, HZG) in collaboration with the Saint Petersburg Electrotechnical University (ETU-LETI). A detailed description of Hereons marine radar is given by Horstmann et al. (2021). The radar system consists of an off-the-shelf X-band (9.48 GHz) marine radar (GEM Leonardo series). Dedicated electronics were added for the digitization and coherentization of the radar signal. The radar is also equipped with a step-motor allowing to steer the antenna in a fixed pointing direction in addition to the standard operation with a rotating antenna. For the present study, the radar was equipped with a 7.5 feet (≈ 2.2 m) antenna

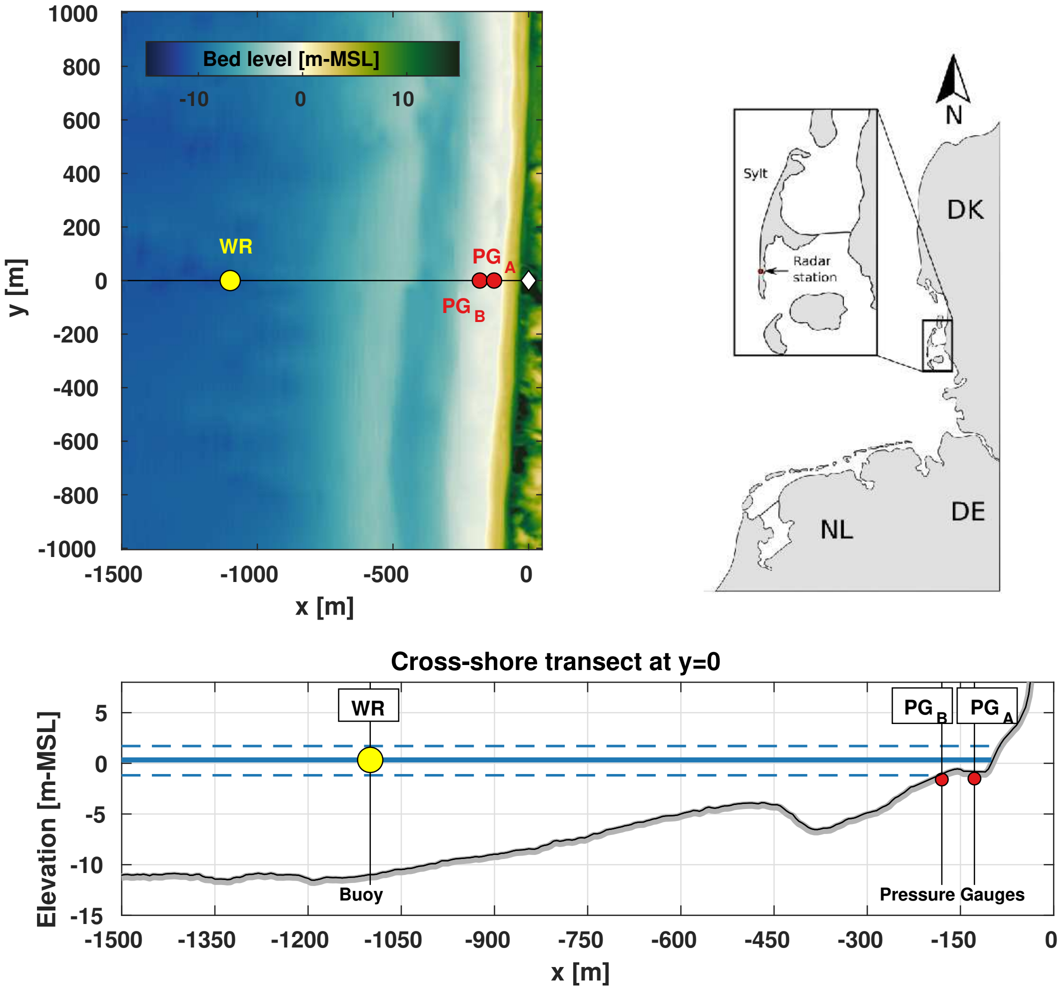

Figure 2. Bathymetry with locations of the Doppler radar (white diamond), the wave rider buoy (yellow dot) and the bottom mounted pressure gauges (red dots). The lower plot shows the cross-shore transect at y=0 m. The blue lines indicate the mean (solid), and minimum/maximum (dashed) water level during the field campaign.

vertically polarized in transmit and receive (VV). It was located approximately 28 m above sea level. The pulse repetition frequency (PRF) was set to 2 kHz with a duration of the transmitted pulses (measured at the half power level) between 50 ns and 70 ns. Analog-to-digital conversion was realized at 80 MHz and then subsampled to 20 MHz corresponding to a sampling range cell spacing of 7.5 m. A total number of 435 range cells were sampled resulting in a maximum range of roughly 3.2 km.

2.1.2 Doppler Signal Processing and Interpretation

Coherent radar measures the amplitude and phase of the received radiation. It facilitates the measurement of the Doppler frequency shift f_D, which is induced by relative motions of the backscattering elements, the scatterers, with respect to the radar antenna. The corresponding Doppler velocity U_D is related to the Doppler frequency shift through the well known Doppler equation

$$U_D = \frac{f_D \, \lambda_{el}}{2 \, \cos\alpha} \, , \tag{1}$$

where λ_{el} is the electromagnetic wave length of the radar signal and α is the projection angle between the scatterer motion and the line-of-sight of the antenna. For the present study, the radar antenna was static, pointing in the cross-shore direction at grazing angles below 10° for the vast majority of the dataset. The Doppler velocity thus represents the cross-shore component of the horizontal scatterer velocity. For X-band radar, the main backscatter from non-breaking parts of the surface is due to Bragg-resonance at the scale of half the radar wave length; hence, the radar measures the horizontal speed of these so called Bragg waves. However, there are further contributions to the Doppler velocity that can complicate its geophysical interpretation. The Doppler velocity may be interpreted as a sum of various components:

$$U_D = U_{Bragg} + U_{curr} + U_{drift} + U_{orb} + U_{break} + U_{graz} \, , \tag{2}$$

where U_{Bragg} is the Bragg waves' phase speed, U_{curr} is the mean current U_{drift} is the a drift velocity due to wind shear and Stokes drift, U_{break} is the contribution of breaking waves and U_{graz} is an additional Doppler shift apparent at grazing incidence. The reason for this additional Doppler shift U_{graz} is still not well understood. It involves complicated interactions of steep waves and shadowing at spatial scales smaller than the radar resolution (Miret et al., 2014), or pulse-smearing artifacts (Streßer et al., 2021). The speed of the Bragg waves U_{Bragg} is constant, U_{curr} and U_{drift} are slowly varying and therefore they are considered as constant over the distance covered by the radar (3 km) and for the typical duration of a radar record (10 min for the present study). The wave orbital motions U_{orb} and the contribution due to breaking U_{break} are varying on smaller temporal and spatial scales. At breaking, the scatterer speed U_{break} is related to parasitic capillary waves at the steep front faces or, for the actively breaking parts, the water mass that is detached from the underlying water body. This can be either the plunging jet of water that forms at incipient breaking or, for spilling breakers, the droplets that are sliding down the font face of the breaker, i.e. surface roller. The roller is moving at a much faster speed as the non-breaking surface in front of it and the magnitude of this spatial difference in scatterer velocity can be used to infer dissipation. This is described in detail in the following section 3.

To estimate the Doppler velocity, Doppler spectra were computed from the complex coherent radar signal for short ensembles of $n = 1024$ consecutive radar pulses. The integration time of one Doppler measurement is thus $dt = 0.512$ s (at PRF = 2000 Hz). The Doppler shift frequency f_D is determined from the location of the Doppler peaks along the frequency axis as described by Streßer et al. (2021). For multi-peaked spectra, only the slowest peak is considered. The velocity of the slower peaks was found to be best suited to trace the non-breaking surface with only minor influence of radar pulse smearing artifacts (Streßer et al., 2021).

3 Radar-Derived Dissipation

3.1 Empirical Scaling

The primary goal in the present work is to find a relationship between the Doppler radar observations and wave dissipation. Microwave radar is very sensitive to the presence of breaking waves and the surface rollers carried by them. When a roller is present within a radar ground cell, the backscatter intensity is significantly increased (e.g. Farquharson et al., 2005; Catalán et al., 2011, 2014). There have been some attempts to relate the observed backscatter either to roller dimensions estimated with the physical optics approximation for scattering from a smooth cylinder (Farquharson et al., 2005) or to the portion of the radar footprint occupied by breakers (Haller & Lyzenga, 2003). A universal model for the radar cross section (RCS) associated with actively breaking waves is still not available. Morever, relating the observed backscatter intensity to RCS requires radiometric calibration for each individual radar, which requires significant effort and is usually not being performed. For this reason we describe a method based on the Doppler velocity rather than RCS.

For actively breaking waves, the radar backscatter originates from the droplets inside the surface roller (e.g. Catalán et al., 2014). Those are moving relatively fast, roughly at the the phase speed c_p of the wave carrying the roller. In the absence of breaking, a much slower scatterer speed is expected, that is closer to the waves' orbital velocity (cf. sec. 2.1.2). Therefore, when the waves are travelling towards the radar, a large increase of the Doppler velocity is expected at the transition from non-breaking to actively breaking parts of the sea surface at the front edge (the toe) of the roller (as visualized in fig. 1). If the difference $dU_D = U_{D,ri+1} - U_{D,ri}$ of the Doppler velocity at the range cell ri+1 and the preceding range cell ri is positive and large, this most likely indicates the transition from non-breaking to breaking parts of the surface. On the contrary, a negative difference is expected at the transition from breaking to non-breaking. However, Streßer et al. (2021) showed that radar pulse smearing can lead to signal artifacts at the rear sides of steep and breaking waves. There is a high chance that Doppler velocity observed in this region is invalid. Therefore, only the positive differences $dU_D > 0$ are considered here and all negative differences are excluded from the computations.

The wave energy dissipation due to wave breaking is is related to the vertical velocity shear. It is determined by the velocity difference between water particle velocity at the surface (within the roller) and the underlying water mass (e.g. Svendsen, 1984). Our hypothesis is thus that the large positive spatial Doppler velocity difference dU_D observed at the toe of surface rollers can be used as a proxy for this vertical velocity difference and is linked to energy dissipation. The following empirical scaling was tested for the radar-derived wave energy dissipation:

$$\overline{D_{emp}} = B_{emp}\ \overline{dU^p}\ , \tag{3}$$

where B_{emp} and the exponent p are calibration constants and the overbar indicates time avaraging over the 10 min long radar record. The empirical calibration constants need to be determined from in-situ observations of the dissipation rate that are deduced from the pressure wave gauges as

$$\overline{D_{PG}} = \frac{F_{PG_B} - F_{PG_A}}{|x_{PG_B} - x_{PG_A}|}\ , \tag{4}$$

where x_{PG_A} and x_{PG_B} are the cross-shore location of the pressure gauges and F_{PG_A} and F_{PG_B} are wave energy flux at each pressure gauge. The wave energy flux is computed as $F_{PG} = \rho_w g\, \overline{\eta_{PG}^2} c_g$, where $c_g = \sqrt{gd}$ is the group speed of the waves (in shallow water equal to the phase velocity), η_{PG} is the surface elevation obtained from the pressure gauges, ρ_w is water density, g is gravitational acceleration, and d is the local water depth. To determine the values empirical constants B_{emp} and p, a cost function is computed representing the root mean square difference between the radar estimate and the observations:

$$F_{cost}(B_{emp},p) = \sqrt{\left(\overline{D_{emp}(B_{emp},p)} - \overline{D_{PG}}\right)^2} \ . \tag{5}$$

For now, only integer values in the range of [1,5] were tested for the exponent p. The minimum of F_{cost} was found for $B_{emp} = 3.65$ kg m^{-3} and $p = 3$, where the difference to the observations was ≈ 17 W m^{-2}. Resulting from dimensional analysis, the unit of B_{emp} must be [kg m^{-3}] to correctly fit to the unit of dissipation [W m^{-2}]. Note, that the empirically derived dissipation rate D_{emp} (eq. 3) was evaluated two radar range cells (15 m) further offshore than the location of the pressure gauges. This is needed because the jump from slow to fast scatterers appears at the toe of the surface roller, but the point where the wave energy is dissipated (the wave crest) is located slightly further offshore. This is explained in more detail in sections 3.2 and 5.

3.2 Physical Scaling

The relationship in eq. 3 is purely empirical and was found from comparisons to the in-situ observations. To gain further insight into the geophysical processes, a derivation based on physical principles is presented in the following. For long-crested waves, the total (bulk) kinetic energy stored in the surface roller per unit span is given by

$$E_{r,total} = \frac{1}{2}\rho' A_r \left(\overline{u_r^2} + \overline{w_r^2}\right) \ , \tag{6}$$

where A_r is the cross-sectional roller area, u_r and w_r are the bulk horizontal and vertical motions of the roller and the overbar indicates time averaging. The bulk density of the roller, including both water and air, can be expressed as

$$\rho' = \beta_\rho \ \rho_w \ , \tag{7}$$

where β_ρ represents the reduction of the water density ρ_w according to the void fraction inside the roller. Phase-averaging the total roller energy yields the roller energy per unit area

$$E_r = \frac{E_{r,total}}{L} \ , \tag{8}$$

where L is the wave length. With the assumption that the vertical component of the roller motion is small ($w_r \ll u_r$), the roller moves approximately with the same speed as the breaking wave, and thus

$$\left(\overline{u_r^2} + \overline{w_r^2}\right) \approx c_p^2 \ . \tag{9}$$

The roller area can be expressed as

$$A_r = \kappa \ HL \ , \tag{10}$$

where H is the wave height and κ is a proportionality constant that varies between 0.06 and 0.07 (Okayasu et al., 1986; Svendsen, 2005). Combining eq. 9, 10, 6 and 8 yields for the roller energy

$$E_r = \frac{1}{2} \ \rho' \ \kappa \ H \ c_p^2 \ . \tag{11}$$

The wave height can not be measured directly by the radar. To substitute H, the dependency of the shallow water wave propagation speed on the wave height (amplitude dispersion) is exploited using the empirical predictor of Booij (1981) for the non-linear shallow water phase speed

$$c_p = \sqrt{g(d + \alpha_{ad} H)} \ . \tag{12}$$

The calibration coefficient α_{ad} determines to what extent the amplitude dispersion is considered. For $\alpha_{ad} = 0$, eq. 12 corresponds to the shallow water phase velocity according to linear wave theory, whereas for $\alpha_{ad} = 0.5$ it corresponds to solitary wave theory. The water depth at the breakpoint can be roughly estimated as

$$d = \frac{H}{\gamma} \ , \tag{13}$$

where γ is the well known breaker parameter which is approximately 0.78. Combining eq. 12 and 13 yields the approximate expression

$$H = \frac{c_p^2}{g\left(\frac{1}{\gamma} + \alpha_{ad}\right)} \ , \tag{14}$$

relating the wave height of a breaking shallow water wave to its phase speed. Combining equations 11, 16 and 14 finally yields a scaling for the roller energy as a function of the phase speed c_p of the breaker

$$E_r = \frac{\beta_\rho \ \kappa \ \rho_w}{2g\left(\frac{1}{\gamma} + \alpha_{ad}\right)} \ c_p^4 \ . \tag{15}$$

The Doppler velocity for the radar cell just before the front edge of the roller is small. For the next radar cell, which is dominated by the roller, the Doppler velocity is close to the phase speed of the breaking wave; thus, the spatial increase in Doppler velocity dU_D can be used to approximate the breaking phase speed as

$$c_p = \beta_D \ dU_D \ . \tag{16}$$

The calibration parameter β_D was introduced to correct for the fact that the positive spatial difference of Doppler velocity dU may not always be an exact estimate of the wave phase speed c_p.

3.2.1 Radar-derived roller properties

Equations 15 and 16 provide the basis to obtain roller properties from the Doppler velocity. To provide a more convenient scaling for the radar-derived roller properties, all calibration parameters within equation 15 are combined to one single scaling factor $B_r = \beta_\rho \ \kappa \ \left(2\left(\gamma^{-1} + \alpha_{ad}\right)\right)^{-1}$ and the final scaling for radar-derived roller energy reads

$$E_r = B_r \ \frac{\rho_w}{g} \ \overline{\left(\beta_D \ dU_D\right)^4} \ , \tag{17}$$

where the over-bar indicates time averaging over the full radar record (10 min for the present study). Accordingly, the flux of roller energy is given by

$$F_r = E_r \ c_p = B_r \ \frac{\rho_w}{g} \ \overline{\left(\beta_D \ dU_D\right)^5} \ . \tag{18}$$

The dissipation of roller energy is related to the roller energy through

$$D_\tau = \frac{2E_r g \beta_s}{c_p}, \tag{19}$$

where β_s is a calibration coefficient related to the slope of the breaking wave front (Deigaard & Fredsøe, 1989; Nairn et al., 1990). Therefore, the scaling for the roller dissipation derived from the radar is

$$D_\tau = 2 \ B_r \ \rho_w \ \overline{\left(\beta_D \ dU_D\right)^3} \ \beta_s \ . \tag{20}$$

All calibration parameters that affect B_r are listed in tab. 1. The assumed default values and the expected minimum and maximum values are also listed for each parameter. The default value for the radar roller dissipation scaling factor is $B_r = 0.0177$. Given the expected ranges of each calibration factor (shown in tab. 1) contributing to B_r, this factor is expected to range within 0.003 and 0.027. The implications of this parameter range for the expected accuracy of the proposed method are discussed in detail in section 7.2.

Parameter	**Symbol**	**Default value**	**Expected range**
Relative roller density	β_ρ	0.9	$[0.3, 0.9]$
Roller area scaling factor	κ	0.07	$[0.06, 0.07]$
Breaker parameter	γ	0.78	$[0.4, 0.88]$
Amplitude dispersion factor	α_{ad}	0.5	$[0.0, 0.5]$
Breaker slope parameter	β_s	0.1	$[0.05, 0.15]$
dU_d to c conversion factor	β_D	1	$[0.7, 1.3]$

Table 1. Dimensionless calibration parameters for the scaling of the radar-derived roller properties.

Note that the empirically found scaling factor that provided the best match with the observations was $B_{emp} = 3.65$ kg m^{-3}. To nondimensionalize the empirical scaling factor, it could also be written in a similar form as as eq. 20, yielding the nondimensional empirical scaling factior $B_{r,emp} = 0.5\ B_{emp}\ \rho_w^{-1}\beta_s^{-1}$. It takes the value 0.0178, which is actually very close to the expected default value of B_r. The similarity between the empirical scaling factor $B_{r,emp}$ and the physically derived scaling factor B_r shows that the two approaches are consistent. This is a strong indication that the assumptions taken do derive the physical scaling are reasonable.

4 Evolution of Roller Dissipation

Figure 3 shows the radar-derived mean roller dissipation D_τ (eq. 20) over the course of the storm. The mean roller dissipation was computed from the hourly 10-min long radar measurements collected in the static antenna mode. Also shown is the significant wave height H_s observed by the wave rider as well as the mean water elevation extracted from the operational model BSHcmod of the German federal hydrographic and maritime traffic agency, that includes the astronomical tide and wind induced surge.

Rollers are present at the outer bar (-800 m $< x < -350$ m) during low tides when $H_s > 1.5$ m. At the peak of the storm, when wave heights reach up to 3 m, the outer bar also remains active during high tide and roller dissipation rates at the crest of the outer bar ($x = -500$ m) reach up to ≈ 120 W m^{-2}. At the inner bar ($x \approx -200$ m, depending on the tide), roller dissipation rates are generally higher and reach values > 200 W m^{-2} over a relatively short distance of less than 100 m. Both, the location and the extent of the inner breaker zone are strongly modulated by the tide. It moves further offshore at low tide when its cross-shore extent is significantly narrower than at high tide. In the swash zone right at the beach face (x $\approx\ -90$ m), rollers are only present at high tide, when the crest of the inter-tidal bar is submerged allowing some wave energy to pass.

5 Cross-shore Transformation of Wave Height

Wave heights in shallow water are strongly influenced by the local water depth. Therefore, the skill of numerical models in predicting nearshore wave heights depends to a large extent on the availability of an up-to-date bathymetry map as well as accurate information on the incident wave energy. This information is often not available and beach profiles can change rapidly, sometimes within a few hours in storm conditions. The proposed radar methodology to obtain roller energy flux and dissipation does not require any additional information. It is therefore interesting to further assess the performance of the radar in comparison to a numerical wave model under optimal preconditions, i.e. a recent bathymetry is available and the incoming wave energy flux is known. The results

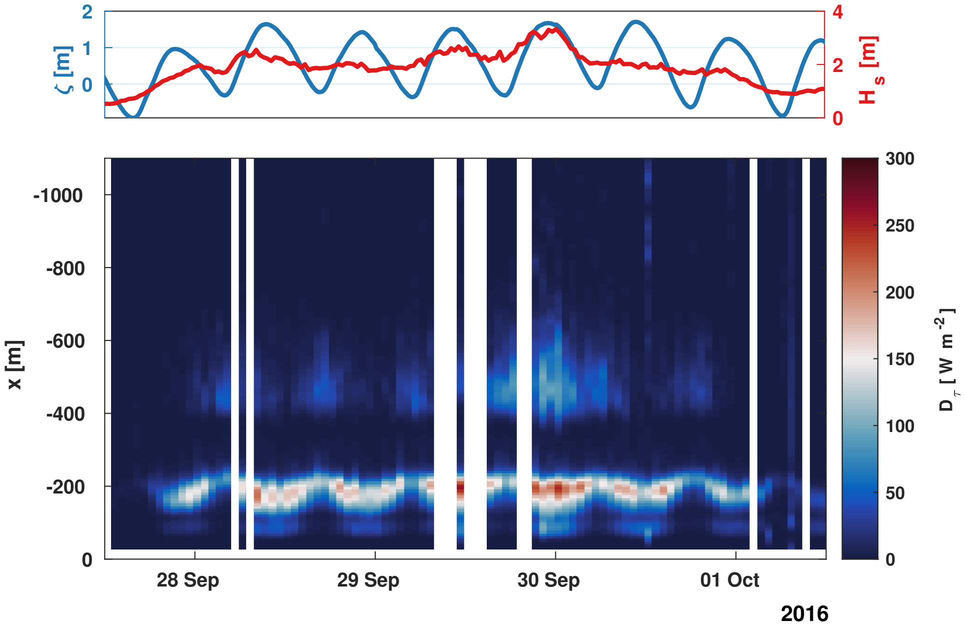

Figure 3. Time-space evolution of radar-derived roller dissipation averaged over 10 minutes at the beginning of each hour. The top panel shows the significant wave height H_s observed by the wave rider buoy and the mean water elevation ζ (tide + surge) from the operational model BSHcmod.

are presented in terms of the significant wave height H_s, which is expected to be more conceivable than the wave energy flux for most readers. The distribution of H_s along the cross-shore transect is computed for both, the radar and the model, using a coupled wave and roller energy flux balance as explained in the following.

For the simplified case of a stationary, unidirectional, normally incident, random wave field, and in the absence of cross-shore currents, the cross-shore wave momentum flux balance can be written as

$$\frac{\partial F_w}{\partial x} = -D_w \ , \tag{21}$$

where $F_w = E_w \, c_g$ is wave energy flux and $E_w = \frac{1}{16}\rho_w g H_s^2$ is the organized wave energy. The source term D_w is the bulk wave energy dissipation. It may be further decomposed into production of turbulence, buoyant air entrainment (bubble generation), sea spray, sound and heat. In equilibrium wave conditions, energy input from winds, dissipation by white-capping and bottom frictional losses cancel each other out. Thus dissipation by depth-induced breaking is the dominant source term in such conditions and is therefore the only one considered for the present study. Svendsen (1984) showed that surface rollers carry a large portion of the total momentum flux in the surf zone. This must be considered in the cross-shore momentum balance. The roller energy is transported towards shore at the phase speed c_p of the wave carrying the roller. Thus, the cross-shore balance of roller energy reads

$$\frac{\partial F_r}{\partial x} = D_w - D_\tau \ , \tag{22}$$

where $F_r = E_r \, c_p$ is the roller energy flux and D_τ is the dissipation of roller energy (eq. 19) and D_w is the wave energy dissipation from eq. 21. The wave dissipation couples eq. 21 with eq. 22. Once wave energy is dissipated, it is transferred to roller energy and is finally dissipated by the shear stress between the roller and the underlying water body.

This generates turbulence and drives wave-induced currents. The roller energy grows or decays according to the difference of D_w and D_τ.

The roller energy E_r, the flux of roller energy F_r, and the dissipation of roller energy D_τ can be directly estimated from the radar measurements using eq. 17, 18 and 20. The dissipation of organized wave energy D_w, at the location x_{ri+1} of the range range cell $ri + 1$ is estimated numerically according to eq. 22 as

$$D_{w,ri+1} = \frac{F_{r,ri} - F_{r,ri+1}}{\Delta r} + D_{\tau,ri} \ , \tag{23}$$

where $\Delta r = x_{ri+1} - x_{ri}$ is the distance between two adjacent radar range cells (here 7.5 m). The wave energy flux at $x_{r,i+1}$ then follows from eq. 21 as

$$F_{w,ri+1} = F_{w,ri} + D_{w,ri} \ \Delta r \ , \tag{24}$$

and the wave energy and significant wave height along the full radar transect are given by

$$E_{w,ri} = \frac{F_{w,ri}}{c_{g,ri}} \tag{25}$$

and

$$H_{s,r_i} = \sqrt{\frac{16 \ E_{w,r_i}}{\rho_w \ g}} \ . \tag{26}$$

The first order numerical integration scheme used in eq. 23 is sensitive to large gradients. Since the radar observations naturally involve some high frequency noise, the radar-derived roller energy (eq. 17), the flux of roller energy (eq. 18) as well as the dissipation of roller energy (eq. 20) were smoothed with a moving average filter spanning 5 range cells to avoid unrealistically high gradients.

For comparison to the radar results, the crosshore wave and roller energy and dissipation was also simulated numerically by solving equations 21 and 22 in the opposite direction, i.e starting offshore. The incoming flux of wave energy at the offshore boundary was derived from the wave rider buoy and the wave dissipation D_w was estimated using the parameterization proposed by Janssen and Battjes (2007) (referred to as JB07, further details can be found in Appendix A).

Figure 4 shows the cross-shore transect of the significant wave height derived from the radar observations (blue line) and the model (red line) at the peak of the storm event, when the offshore significant wave height was 3.2 m with a peak period of 10 s. Also shown are the cross-shore distributions of observed and simulated wave and roller dissipation, as well as the beach profile. The H_s-profile obtained from the radar yields a realistic cross-shore distribution of H_s. It is very similar to the result from the simulation for this situation. The observed wave height at all available in-situ sensors, the pressure wave gauges $\mathrm{PG_A}$ and $\mathrm{PG_B}$, and the wave rider buoy is matched well. The radar slightly underestimates the wave height that is observed at $\mathrm{PG_B}$ ($x = -180$ m), whereas the model seems to match the in-situ observations better at this location. The reason for this can be seen in the center panel of fig. 4. The wave dissipation rate D_w observed by the radar just offshore of $\mathrm{PG_B}$ (≈ 280 W m^{-2}) is significantly higher than the one predicted by the model (≈ 190 W m^{-2}). Accordingly, the radar-derived wave height decreases faster in this region compared to the simulation. The transition region after onset of breaking until the point when the rollers have formed is still not well understood and the assumption of an analogy between breaking waves and a moving bore within the JB07 parameterization is violated. It is therefore possible, that the radar observations provide a more realistic estimate for the wave dissipation in this transition region, but further ground truth with better spatial coverage would be needed to investigate this. However, it is interesting that the observed and the simulated roller dissipation D_τ in the region of the inner bar have similar magnitudes. This shows nicely that the formation of surface rollers

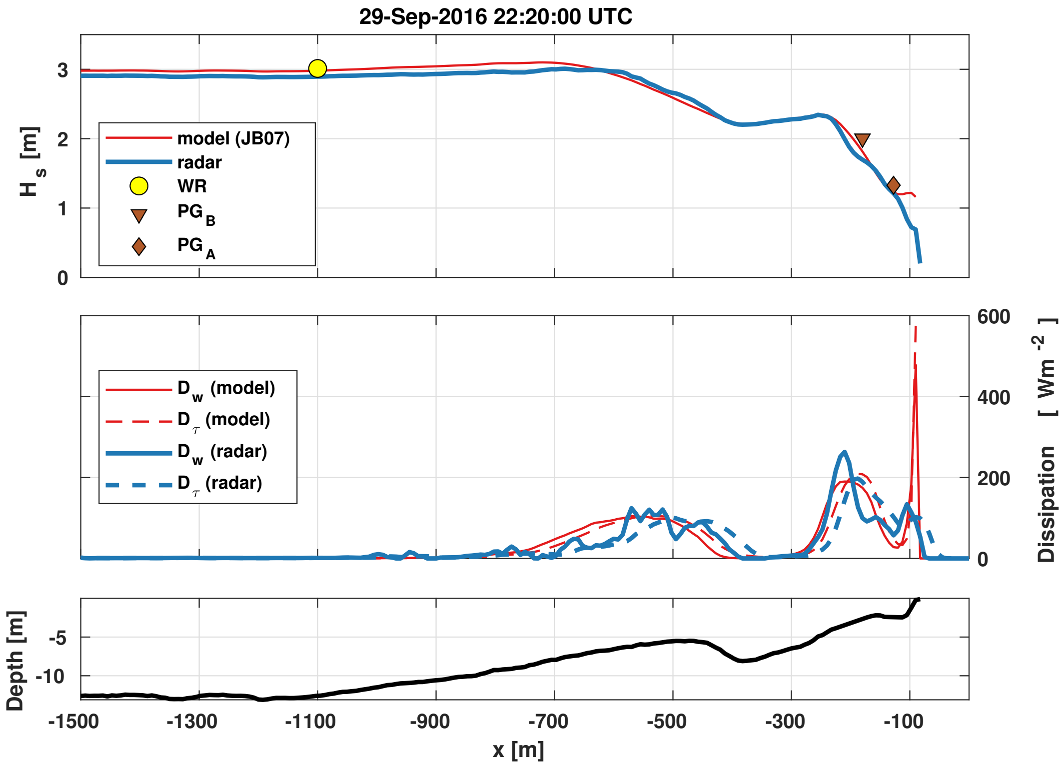

Figure 4. Top: Cross-shore transformation of the significant wave height H_s at the peak of the storm (Sep. 29,2016 22:20 UTC) as observed by the radar (blue) and simulated with the parameterization of Janssen and Battjes (2007) (JB07, red). Also shown are in-situ observations at the wave rider buoy (WR, yellow circle) and the pressure gauges $\mathrm{PG_B}$ (brown triangle) as well as $\mathrm{PG_A}$(brown diamond). Center: Observed (blue) and simulated (red) dissipation of organized wave energy D_w and roller dissipation D_τ. Bottom: Depth profile at the time of the measurements.

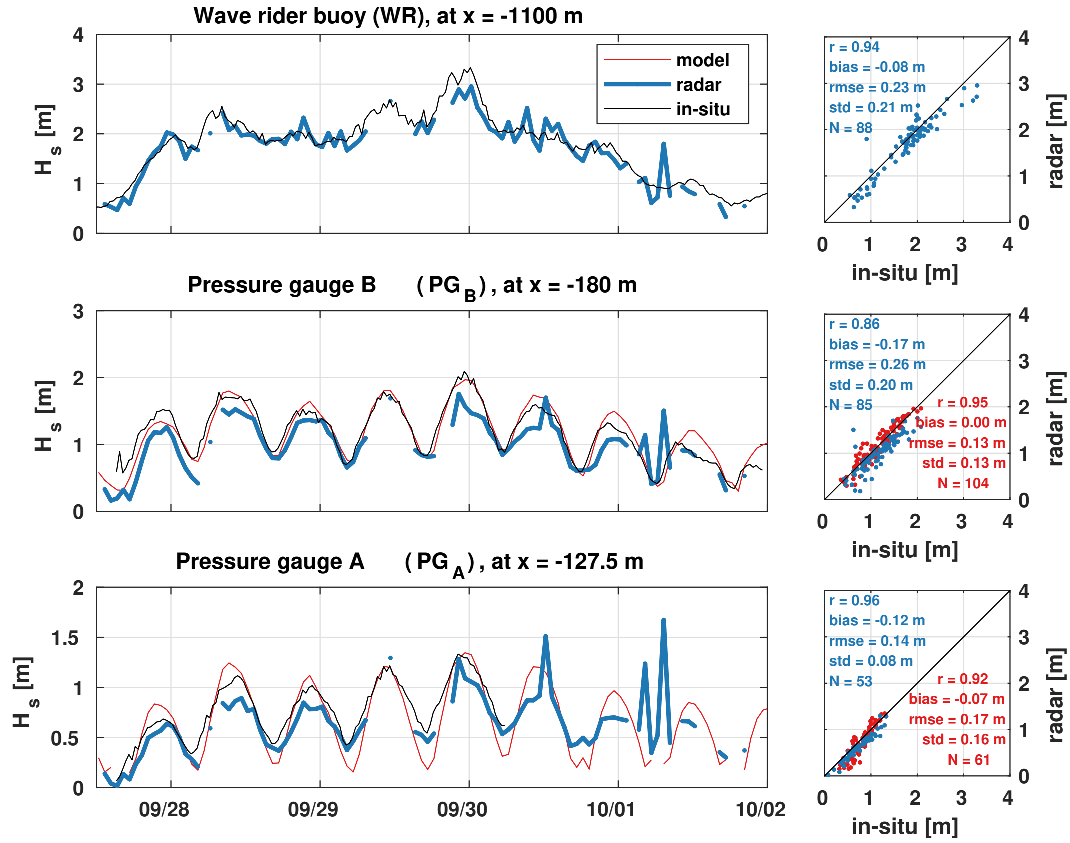

Figure 5. Time series of significant wave height observed by the radar (blue), simulated by the model (red) and in-situ observations (black) at the locations of the in-situ sensors, i.e. the wave rider buoy (WR), and the two bottom mounted pressure wave gauges PG_B and PG_A. The right panels show the corresponding scatter diagrams of H_s and error statistics.

compensates abrupt changes in wave dissipation leading to a smoothing and and onshore shift of the forcing of wave-induced currents (e.g. Goda, 2006).

To better quantify the overall performance of the proposed method, error statistics are computed for the locations where in-situ data is available. Figure 5 shows the time series of the observed and the simulated significant wave heights at the wave rider buoy (WR) and the two bottom mounted pressure wave gauges (PG_B and PG_A). Also shown are the corresponding scatter diagrams and error metrics. Both, the radar observations and the simulations are matching the in-situ measurements well at all three locations throughout the entire storm event. The root-mean square errors (RMSE) and corresponding bias (in parenthesis) of the radar observations (blue colors) are 0.14 m (-0.12 m), 0.26 m (-0.17 m), and 0.23 m (-0.08 m), at PG_A, PG_B and WR, respectively. The combined RMSE (bias) taking all available sensors into account is 0.23 m (-0.13 m). While the results are generally very good during a growing sea, a slight decrease in the performance is apparent in the decaying phase of the storm. The wave model shows a slightly smaller deviation from the ground truth with RMSEs (biases) of 0.17 m (-0.07 m) and 0.13 m (0.00 m) at PG_A and PG_B, respectively. Since the wave model was forced at the offshore boundary with the observed wave height at the buoy, it makes no sense to compute an error at this location. Even if the wave model appears to be performing slightly better, the skill of the proposed radar method and the wave model in estimat-

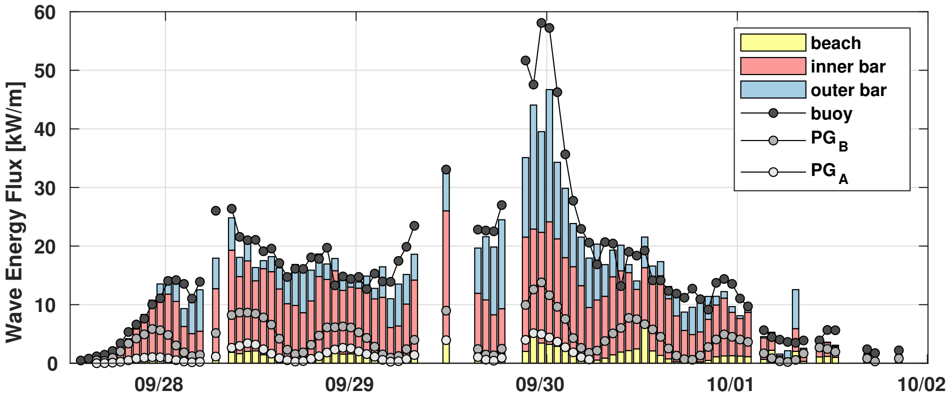

Figure 6. Flux of incoming wave energy measured at the wave rider buoy and the pressure gauges ($\mathrm{PG_B}$ and $\mathrm{PG_A}$) together with the radar-derived wave energy flux represented by the bars in the plot. The color coding indicates the energy flux dissipated at the outer bar (between $x = -1100$ m and $x = -330$ m, light blue), the inner bar (between $x = -330$ m and $x = -127.5$ m, light red) and the swash zone at the beach (between $x = -127.5$ m and $x = 0$ m, light yellow).

ing the significant wave height is comparable. The results show that the proposed radar method can be applied with similar accuracy as numerical wave models, but without the need to know the bathymetry or incident wave height. This is a major benefit in particular for long-term observations.

6 Energy Flux Budget

The radar provides measurements of wave energy flux and dissipation along the complete cross-shore transect every 7.5 m over a distance of more than 1.5 km. This opens the opportunity to quantify and attribute the dissipation of wave energy to different morphological features, the outer bar, the inner bar and the swash zone at the beach. Figure 6 shows the in-situ measurements of the incoming flux of wave energy at the wave rider buoy and the two pressure gauges $\mathrm{PG_A}$ and $\mathrm{PG_B}$. The bars in the plot represent the radar-derived flux of wave energy, separated into the portion of energy dissipated at the outer bar, the inner bar, and the swash zone at the beach. At the peak of the storm, when $H_s > 3$ m at the buoy, about 50% of the total incoming wave energy flux is already dissipated at the outer sandbar. This nicely demonstrates the effectiveness of submerged morphological features in reducing the wave energy at the beach during storm conditions. The energy that ends up at the beach shows a dependency on tides, but not so much on the offshore wave height, indicating the expected strong bathymetric control of the nearshore wave heights.

7 Discussion

The results presented in sections 5 and 6 show a good performance of the method over the entire storm event, and the complete cross-shore transect. Previous radar-based wave height retrieval methods based on the signal-to-noise ratio or a direct inversion of the Doppler velocity to surface elevation often fail in the nearshore due to the high spatial variability and high wave non-linearity. The proposed method now provides a radar-based close-range remote sensing technique to reliably observe the transformation of wave energy in the surf zone at a spatial high resolution ($dx = 7.5$ m). Such measurements are complicated to realize using traditional point observation based wave monitoring systems, e.g. arrays of wave buoys, bottom mounted ADCPs or pressure wave gauges.

Furthermore, for many research questions the surface stress is the quantity of interest because it is directly driving wave-induced currents and turbulence production by breakers (e.g. Svendsen, 2005). The primary quantity that is observed by the radar is the roller energy and dissipation, which is closely related to the Reynolds stress acting at the water surface. Estimating roller quantities, as done here, is therefore a more direct measure of the drivers of nearshore circulation compared to wave height measurements.

A small disadvantage is the fact that the wave height must be known for at least one location along the transect. This is not a problem, if the beach (where there is no wave energy) is located inside the area covered by the radar. However, it could be problematic e.g. in reef-lagoon systems where the wave energy does not drop to zero inside the lagoon. Another requirement for the method is the fact that the jump from slow to fast Doppler speeds at the toe of the breaker must be visible. If the dominant wave length of the wave field is short and the local grazing angle is low, the entire wave trough might be shadowed. In this situation, it would not possible to estimate the Doppler velocity at the toe of the roller and thus dU_D is not anymore related to the wave phase speed c_p. The dissipation rate would then be strongly underestimated. Adjusting β_D to compensate underestimation of c_p would not help in this case because the error stems from missing information rather than from a systematic bias. For the studied storm event, however, there was no indication for an error of this kind. However, the lower limits of the method in terms of wave length and local grazing angle remain to be determined in future studies.

7.1 Generalisation and transferability

The roller concept was originally introduced for spilling breakers in deep water (Duncan, 1981). From laboratory experiments, Duncan (1981) found that the height of breaking deep water waves scales with

$$H = 0.6 \, \frac{c_p^2}{g} \; . \tag{27}$$

In the present work, eq. 14 was used to substitute the wave height. This scaling is only valid for breaking waves in shallow water. However, the chosen typical values for γ and α_{ad} within eq. 14 yield

$$H = \frac{c_p^2}{g\left(\frac{1}{0.78} + 0.5\right)} = 0.5612 \, \frac{c_p^2}{g} \approx 0.6 \, \frac{c_p^2}{g} \; , \tag{28}$$

and thus match the results of Duncan (1981). This suggests that the proposed scaling is also valid for breaking deep water waves. However, further research is required to confirm this assumption.

Another question that remains open is whether the proposed scaling also provides good results in the transition region between the onset of breaking and the formation of the roller. In this region, the roller concept does not describe the physics well. It is missing important aspects such as the formation plunging jet of water and the corresponding energy transfer when the jet hits the surface. This is expected to be of higher relevance for a plunging breaker type, since for spilling breakers, the roller is formed faster. The roller concept was utilized in the context of the present study to provide a physical basis for the proposed scalings to obtain roller energy (eq. 17) and dissipation (eq. 20) from the Doppler velocity measured by the radar. However, the empirically derived scaling given (eq. 3) does not rely on the roller concept. Due to its empirical nature, it must not necessarily be invalid in this region and could potentially also provide good data there. More in-situ data in particular with higher spatial coverage and resolution in the transition region is needed to investigate this hypothesis.

7.2 Uncertainty

Two main sources of uncertainty can affect the radar-based estimation of roller energy. Firstly, the correct value of the physically motivated calibration parameter B_r is not exactly known. Secondly, the spatial increase of the Doppler velocity dU_d may not always exactly represent the wave phase speed c_p.

The condensed calibration parameter B_r (in eq. 17, 18, and 20) is composed of multiple components. Each calibration parameter within B_r has a specific physical meaning and default values were selected from well accepted approximations available from literature. However, the majority of these parameters stem from empirical studies and may need to be calibrated for each individual location. Moreover, some parameters e.g. the air fraction within the roller represented by β_ρ as well as the roller area scaling factor κ are very difficult to determine in the field. The combined scaling factor B_r should therefore be interpreted as a general calibration factor for the proposed method. It yields very good results for the environmental conditions of the present study, but may need to be adjusted elsewhere. As discussed above, it is likely that different breaker types require different choices for B_r to compensate for errors due to aspects of the physics that are not covered by the roller concept. As mentioned in section 3.2, the estimated lower and upper bounds of the radar roller dissipation scaling factor B_r are 0.003 and 0.027, respectively. However, since these limits reflect the largest expected deviations from the correct value of B_r, it is assumed that the appropriate value for B_r is much closer to the default value of 0.0177 in most conditions.

The calibration factor β_D was introduced to compensate the second source of error, i.e. a discrepancy between the measured spatial increase in Doppler velocity dU_D and wave phase speed c_p. For the present study, β_D was set to 1 implying the assumption $dU_D = c_p$. However, environmental conditions such as the sea state, the wind and also the radar installation height may affect the correct choice of β_D. A systematic analysis of the dependency of β_D on these external factors may result in a reduction of uncertainty in future.

The present data set does not provide sufficient ground truth to perform an empirical quantification of the measurement uncertainty. Instead, a brief discussion of the theoretical uncertainties and their implications is provided here. The expected range of β_D from 0.7 to 1.3 implies an error of $\pm 30\%$ for the estimation of wave phase speed (i.e. $c_p = (1 \pm 0.3)\ dU_D$). Since the wave dissipation scales with dU^3 (see eq. 23), error propagation yields an uncertainty of 90% for *individual* measurements of the dissipation. However, for the mean dissipation over one 10-min radar record, this error will be significantly reduced due to averaging. The integration time of 0.512 s for the Doppler velocity yields $N = 1170$ measurements of dU_D during the 10-min sampling. If all measurements were independent and there was no bias, the error would be reduced by a factor of $1170^{-0.5}$ resulting in an approximate relative error for the mean dissipation and roller energy of 2.6% and 3.5%, respectively. However, it is unlikely that all measurements of dU_D are independent particularly if they belong to the same individual wave. A better assumption could be to consider the number of waves in the record instead of the number of samples. The peak period measured by the wave rider buoy is 10 s meaning approximately 60 waves are observed during a 10-min long radar record. This translates to maximum expected relative accuracy of 11.6 % and 15.5 % for the mean dissipation and roller energy, respectively.

8 Summary and Conclusion

High-resolution (7.5 m) observations of surface wave and roller dissipation are studied along a cross-shore transect of a submesotidal, double-barred, sandy beach in the Southern North Sea. A new close-range remote sensing methodology is introduced to estimate surface roller energy and dissipation from coherent-on-receive marine radar backscatter. Ground truthing observations of the dissipation of waves breaking over an intertidal sandbar were estimated between the location of two bottom mounted pressure wave gauges. It is shown empirically, that the spatial increase of the Doppler velocity observed by the radar at the transition from non-breaking to breaking parts of the sea surface is related to the observed dissipation rate. This empirical relationship can be explained with the concept of surface rollers combined with common approximations for nearshore breaking waves. Based on this physical concept, scalings are derived to directly estimate the energy stored within surface rollers, the dissipation of roller energy, and the flux of roller energy from the Doppler velocity observed by the radar. Assimilation of these quantities into the coupled, one-dimensional wave and roller energy flux balance equations also yields the dissipation and energy flux (and thus the significant wave height) of organized wave energy along a cross-shore transect over more than one kilometer with a spatial resolution of 7.5 m. Comparisons to the in-situ observations at the two pressure gauges and a wave rider buoy, moored about 1 km off the shoreline, indicate a good performance of the proposed method. Root-mean-square errors at all locations were below 0.26 m over the course of a storm lasting three days, with significant wave heights peaking at 3.3 m. Results from a phase-averaged numerical wave model showed errors below 0.15 m and thus the skill of the radar observation is slightly lower, but comparable to the model. However, no prior knowledge of the bathymetry is required for the radar-based estimates. This is a major benefit compared to numerical wave models, in particular for locations where rapid bathymetric changes occur, e.g. sandy beaches. This new methodology overcomes the difficulties of previously available radar-based wave height retrieval methods, that are not able to provide reliable measurements in the surf zone, mostly due to the influence of wave breaking and and increased spatial inhomogeneity. Strong rain and the absence of surface roughness due to low winds are expected to negatively influence the method. However, shore-based radar is relatively easy to install and maintain and is able to measure day and night as well as in foggy conditions. This makes the technology perfectly suited for continuous long-term observations with high spatial and temporal resolution, that are difficult to realize with in-situ instrumentation.

The observations are used to investigate wave transformation along a double-barred beach profile and attribute wave energy losses to the morphological features, i.e the outer bar, the inner bar, and the swash zone. Highest roller dissipation rates (> 200 W m^{-2}) are found at the inner bar, where also the majority of the incoming wave energy flux is dissipated during moderate conditions. In storm conditions, however, up to 50% of the wave energy is dissipated at the outer bar. This confirms the effectiveness of submerged bathymetric features in reducing wave heights at the beach in energetic wave conditions.

Appendix A JB07 wave breaking parameterization

The wave breaking parameterization proposed by Janssen and Battjes (2007) (referred to as JB07) approximates the average dissipation of wave energy per unit surface area by depth induced breaking as

$$D_{JB} = \frac{3\sqrt{\pi}}{16}\ B\ f_{rep}\ \rho g\ \frac{H_{rms}^3}{d}\left[1 + \frac{4}{3\sqrt{\pi}}\left(R^3 + \frac{3}{2}R\right)\exp\left[R^2\right] - \mathrm{erf}(R)\right]\ , \tag{A1}$$

where $R = H_b/H_{rms}$, $H_b = \gamma d$ and B is a calibration factor representing the breaking strength and is set to one. f_{rep} is the representative frequency of the wave field (often the peak frequency is considered). JB07 includes a slight modification of the empirical relationship for the breaker parameter proposed by Battjes and Stive (1985)

$$\gamma = \frac{H_b}{d} = 0.39 + 0.56\ \tanh(33\ S_0)\ , \qquad \text{(A2)}$$

which depends on the offshore wave steepness $S_0 = (H_{rms}/L)_{\text{offshore}}$. JB07 is similar to an earlier parameterization by Baldock et al. (1998). However, in JB07 the H^3/d dependency is retained instead of substituting it by H^2, as done by Baldock et al. (1998), who assumed that the wave height of a breaking is approximately equal to the water depth, as proposed by Battjes and Janssen (1978). The same modification was coincidentally also reported by Alsina and Baldock (2007) in the same year.

Acknowledgments

This work was funded by the Helmholtz Association through the program Polar Regions and Coasts in the Changing Earth System (PACES II).

The authors would like to thank Dr. Grant Deane, Dr. Jörg Seemann, Marius Cysewski and Ruben Carrasco for fruitful discussions that have helped to improve the quality of the manuscript. Technical support by Jan Bödewadt and Jurij Stell is highly appreciated. Many thanks to Jens Winkelbauer and Prof. Dr. Peter Fröhle from the Technical University of Hamburg (TUHH) for sharing the design of the pressure loggers. We also acknowledge the support of the "Landesbetrieb für Küstenschutz, Nationalpark und Meeresschutz Schleswig-Holstein" (LKN.SH) in providing the laser scan topography data, and the "Bundesamt für Seeschifffahrt und Hydrographie" (BSH) for extracting the water levels and currents from the operational models.

Open Research

The wave rider buoy data is available from the COSYNA data portal at `http://codm.hzg.de/codm`. The bathymetry data is available from the PANGAEA data portal at `https://doi.org/10.1594/683PANGAEA.898407`. The pressure transducer time series will be available from the PANGAEA data portal (submitted, doi requested). Post-processed radar observations, wave model results and ground truth used in this study are available from the Zenodo repository at `https://doi.org/10.5281/zenodo.5787131`. Radar raw data is available from the authors on request.

References

Aarninkhof, S. G. J., & Ruessink, B. G. (2004). Video observations and model predictions of depth-induced wave dissipation. *IEEE Transactions on Geoscience and Remote Sensing*, *42*(11), 2612–2622. doi: 10.1109/TGRS.2004.835349

Aarninkhof, S. G. J., Ruessink, B. G., & Roelvink, J. A. (2005). Nearshore subtidal bathymetry from time-exposure video images. *Journal of Geophysical Research: Oceans*, *110*(6), 1–13. doi: 10.1029/2004JC002791

Alsina, J. M., & Baldock, T. E. (2007). Improved representation of breaking wave energy dissipation in parametric wave transformation models. *Coastal Engineering*, *54*(10), 765–769. doi: 10.1016/j.coastaleng.2007.05.005

Baldock, T., Holmes, P., Bunker, S., & Van Weert, P. (1998, sep). Cross-shore hydrodynamics within an unsaturated surf zone. *Coastal Engineering*, *34*(3-4), 173–196. Retrieved from `https://linkinghub.elsevier.com/retrieve/pii/S0378383998000179` doi: 10.1016/S0378-3839(98)00017-9

Battjes, J. A., & Janssen, J. P. F. M. (1978, aug). Energy Loss and Set-Up Due to Breaking of Random Waves. In *Coastal engineering 1978* (Vol. 91, pp. 569–587). New York, NY: American Society of Civil Engineers. Retrieved from http://ascelibrary.org/doi/10.1061/9780872621909.034 doi: 10.1061/9780872621909.034

Battjes, J. A., & Stive, M. J. F. (1985). Calibration and verification of a dissipation model for random breaking waves. *Journal of Geophysical Research*, *90*(C5), 9159. Retrieved from http://doi.wiley.com/10.1029/JC090iC05p09159 doi: 10.1029/JC090iC05p09159

Bell, P. S., & Osler, J. C. (2011). Mapping bathymetry using X-band marine radar data recorded from a moving vessel. *Ocean Dynamics*, *61*(12), 2141–2156. doi: 10.1007/s10236-011-0478-4

Bergamasco, F., Torsello, A., Sclavo, M., Barbariol, F., & Benetazzo, A. (2017). WASS: An open-source pipeline for 3D stereo reconstruction of ocean waves. *Computers and Geosciences*, *107*(June), 28–36. Retrieved from http://dx.doi.org/10.1016/j.cageo.2017.07.001 doi: 10.1016/j.cageo.2017.07.001

Bonneton, P., Lannes, D., Martins, K., & Michallet, H. (2018, aug). A nonlinear weakly dispersive method for recovering the elevation of irrotational surface waves from pressure measurements. *Coastal Engineering*, *138*(June 2017), 1–8. Retrieved from https://doi.org/10.1016/j.coastaleng.2018.04.005https://linkinghub.elsevier.com/retrieve/pii/S0378383917302892 doi: 10.1016/j.coastaleng.2018.04.005

Booij, N. (1981). *Gravity waves on water with non-uniform depth and current.* (Unpublished doctoral dissertation). TU Delft.

Brown, G. (1998, jan). Guest Editorial - Special Issue On Low-grazing-angle Backscatter From Rough Surfaces. *IEEE Transactions on Antennas and Propagation*, *46*(1), 1–2. Retrieved from http://ieeexplore.ieee.org/document/655445/ doi: 10.1109/TAP.1998.655445

Carini, R. J., Chickadel, C. C., Jessup, A. T., & Thompson, J. (2015). Estimating wave energy dissipation in the surf zone using thermal infrared imagery. *Journal of Geophysical Research: Oceans*, *120*(6), 3937–3957. doi: 10.1002/2014JC010561.Received

Carrasco, R., Horstmann, J., & Seemann, J. (2017). Significant Wave Height Measured by Coherent X-Band Radar. *IEEE Transactions on Geoscience and Remote Sensing*, *55*(9), 5355–5365. doi: 10.1109/TGRS.2017.2706067

Catalán, P. A., Haller, M. C., Holman, R. A., & Plant, W. J. (2011). Optical and microwave detection of wave breaking in the surf zone. *IEEE Transactions on Geoscience and Remote Sensing*, *49*(6 PART 1), 1879–1893. doi: 10.1109/TGRS.2010.2095864

Catalán, P. A., Haller, M. C., & Plant, W. J. (2014, may). Microwave backscattering from surf zone waves. *Journal of Geophysical Research: Oceans*, *119*(5), 3098–3120. Retrieved from http://doi.wiley.com/10.1002/2014JC009880 doi: 10.1002/2014JC009880

Chernyshov, P., Vrecica, T., Streßer, M., Carrasco, R., & Toledo, Y. (2020, apr). Rapid wavelet-based bathymetry inversion method for nearshore X-band radars. *Remote Sensing of Environment*, *240*(May 2019), 111688. Retrieved from https://doi.org/10.1016/j.rse.2020.111688https://linkinghub.elsevier.com/retrieve/pii/S0034425720300572 doi: 10.1016/j.rse.2020.111688

Chickadel, C. C., Holman, R. A., & Freilich, M. H. (2003). An optical technique for the measurement of longshore currents. *Journal of Geophysical Research: Oceans*, *108*(11), 1–17. doi: 10.1029/2003jc001774

Cysewski, M., Streßer, M., Bödewadt, J., Perthun, P., Carrasco, R., & Horstmann, J. (2019, feb). *Single beam bathymetry transects at the West coast of Sylt from Sep 22-26 2016.* PANGAEA. Retrieved from https://doi.org/10.1594/PANGAEA.898407 doi: 10.1594/PANGAEA.898407

Deigaard, R., & Fredsøe, J. (1989, dec). Shear stress distribution in dissipative water waves. *Coastal Engineering*, *13*(4), 357–378. Retrieved from https://linkinghub.elsevier.com/retrieve/pii/0378383989900422 doi: 10.1016/0378-3839(89)90042-2

Díaz, H., Catalán, P. A., & Wilson, G. W. (2018). Quantification of two-dimensionalwave breaking dissipation in the surf zone from remote sensing data. *Remote Sensing*, *10*(1), 1–17. doi: 10.3390/rs10010038

Dick, S. (2001). *The Operational Circulation Model of BSH(BSHcmod): Model Description and Validation.* Hamburg: BSH.

Dugan, J. P., Piotrowsky, C. C., Williams, J. Z., Piotrowski, C. C., & Williams, J. Z. (2001). Water depth and surface current retrievals from airborne optical measurements of surface gravity wave dispersion. *Journal of Geophysical Research*, *106*(C8), 16903–16915. doi: 10.1029/2000JC000369

Duncan, J. H. (1981, jul). An experimental investigation of breaking waves produced by a towed hydrofoil. *Proceedings of the Royal Society of London. A. Mathematical and Physical Sciences*, *377*(1770), 331–348. Retrieved from https://royalsocietypublishing.org/doi/10.1098/rspa.1981.0127 doi: 10.1098/rspa.1981.0127

Farquharson, G., Frasier, S. J., Raubenheimer, B., & Elgar, S. (2005). Microwave radar cross sections and Doppler velocities measured in the surf zone. *Journal of Geophysical Research: Oceans*, *110*(12), 1–12. doi: 10.1029/2005JC003022

Flores, R. P., Catalán, P. A., & Haller, M. C. (2016, aug). Estimating surfzone wave transformation and wave setup from remote sensing data. *Coastal Engineering*, *114*(April), 244–252. Retrieved from http://dx.doi.org/10.1016/j.coastaleng.2016.04.008https://linkinghub.elsevier.com/retrieve/pii/S0378383916300497 doi: 10.1016/j.coastaleng.2016.04.008

Goda, Y. (2006). Examination of the influence of several factors on longshore current computation with random waves. *Coastal Engineering*, *53*(2-3), 157–170. doi: 10.1016/j.coastaleng.2005.10.006

Haller, M. C., & Lyzenga, D. R. (2003). Comparison of radar and video observations of shallow water breaking waves. *Ieee Transactions on Geoscience and Remote Sensing*, *41*(4), 832–844. doi: Doi10.1109/Tgrs.2003.810695

Holman, R., & Haller, M. C. (2013). Remote Sensing of the Nearshore. *Annual Review of Marine Science*, *5*(1), 95–113. Retrieved from http://www.annualreviews.org/doi/10.1146/annurev-marine-121211-172408 doi: 10.1146/annurev-marine-121211-172408

Holman, R., Plant, N., & Holland, T. (2013, may). cBathy: A robust algorithm for estimating nearshore bathymetry. *Journal of Geophysical Research: Oceans*, *118*(5), 2595–2609. Retrieved from http://doi.wiley.com/10.1002/jgrc.20199 doi: 10.1002/jgrc.20199

Horstmann, J., Bödewadt, J., Carrasco, R., Cysewski, M., Seemann, J., & Streβer, M. (2021, nov). A Coherent on Receive X-Band Marine Radar for Ocean Observations. *Sensors*, *21*(23), 7828. Retrieved from https://www.mdpi.com/1424-8220/21/23/7828 doi: 10.3390/s21237828

Horstmann, J., Borge, J. C. N., Seemann, J., Carrasco, R., & Lund, B. (2015). Wind, Wave, and Current Retrieval Utilizing X-Band Marine Radars. In *Coastal ocean observing systems* (pp. 281–304). Elsevier. Retrieved from https://linkinghub.elsevier.com/retrieve/pii/B978012802022700016X doi: 10.1016/B978-0-12-802022-7.00016-X

Huang, W., Liu, X., & Gill, E. (2017, dec). Ocean Wind and Wave Measurements Using X-Band Marine Radar: A Comprehensive Review. *Remote Sensing*, *9*(12), 1261. Retrieved from http://www.mdpi.com/2072-4292/9/12/1261 doi: 10.3390/rs9121261

Janssen, T., & Battjes, J. (2007, sep). A note on wave energy dissipation over steep beaches. *Coastal Engineering*, *54*(9), 711–716. Retrieved from https://linkinghub.elsevier.com/retrieve/pii/S0378383907000580 doi: 10.1016/j.coastaleng.2007.05.006

LKN.SH. (2015). *Fachplan Küstenschutz Sylt Historisches zur Entwicklung der Insel Sylt (Einleitung).*

Lund, B., Haus, B. K., Horstmann, J., Graber, H. C., Carrasco, R., Laxague, N. J. M., . . . Özgökmen, T. M. (2018, may). Near-Surface Current Mapping by Shipboard Marine X-Band Radar: A Validation. *Journal of Atmospheric and Oceanic Technology*, *35*(5), 1077–1090. Retrieved from https://journals.ametsoc.org/view/journals/atot/35/5/jtech-d-17-0154.1.xml doi: 10.1175/JTECH-D-17-0154.1

Martins, K., Blenkinsopp, C. E., Deigaard, R., & Power, H. E. (2018). Energy Dissipation in the Inner Surf Zone: New Insights From LiDAR-Based Roller Geometry Measurements. *Journal of Geophysical Research: Oceans*, 3386–3407. doi: 10.1029/2017JC013369

Martins, K., Blenkinsopp, C. E., & Zang, J. (2016). Monitoring individual wave characteristics in the inner surf with a 2-dimensional laser scanner (LiDAR). *Journal of Sensors*, *2016*. doi: 10.1155/2016/7965431

McGregor, J. A., Poulter, E. M., & Smith, M. J. (1998). S band Doppler radar measurements of bathymetry, wave energy fluxes, and dissipation across an offshore bar. *Journal of Geophysical Research: Oceans*, *103*(C9), 779–789. doi: 10.1029/98JC00447

Miret, D., Soriano, G., Nouguier, F., Forget, P., Saillard, M., & Guerin, C. A. (2014). Sea surface microwave scattering at extreme grazing angle: Numerical investigation of the doppler shift. *IEEE Transactions on Geoscience and Remote Sensing*, *52*(11), 7120–7129. doi: 10.1109/TGRS.2014.2307893

Nairn, R., Roelvink, J. A., & Southgate, H. (1990). Transition zone width and implications for modeling surfzone hydrodynamics. *Proceedings 22th International Conference on Coastal Engineering*, 68–81. doi: 10.9753/icce.v22.

Navarro, W., Orfila, A., Orejarena-Rondón, A., Velez, J. C., & Lonin, S. (2021, nov). Wave Energy Dissipation in a Shallow Coral Reef Lagoon Using Marine X-Band Radar Data. *Journal of Geophysical Research: Oceans*, *126*(11), 1–23. Retrieved from https://onlinelibrary.wiley.com/doi/10.1029/2020JC017094 doi: 10.1029/2020JC017094

Navarro, W., Velez, J. C., Orfila, A., & Lonin, S. (2019). A shadowing mitigation approach for sea state parameters estimation using X-band remotely sensing radar data in coastal areas. *IEEE Transactions on Geoscience and Remote Sensing*, *57*(9), 6292–6310. doi: 10.1109/TGRS.2019.2905104

Nieto Borge, J. C., Hessner, K., & Reichert, K. (1999). Estimation of the Significant Wave Height With X-Band Nautical Radars. *Proc. 18th Int. Conf. Offshore Mech*(C), 1–8. Retrieved from http://scholar.google.com/scholar?hl=en{\&}btnG=Search{\&}q=intitle:ESTIMATION+OF+THE+SIGNIFICANT+WAVE+HEIGHT+WITH+X-BAND+NAUTICAL+RADARS{\#}0

Nieto Borge, J. C., Rodríguez Rodríguez, G., Hessner, K., & González Izquerdo, P. (2004). Inversion of marine radar images for surface wave analysis. *Journal of Atmospheric and Oceanic Technology*, *21*(8), 1291–1300. doi: 10.1175/1520-0426(2004)021⟨1291:IOMRIF⟩2.0.CO;2

Okayasu, A., Shibayama, T., & Mimura, N. (1986). Velocity Field under Plunging Waves. *Coastal Engineering 1986*, 660–674. Retrieved from http://ascelibrary.org/doi/10.1061/9780872626003.050 doi: 10.1061/9780872626003.050

Plant, W. J., Keller, W. C., & Cross, A. (1983). Parametric dependence of ocean wave- radar modulation transfer functions. *Journal of Geophysical Research*, *88*(C14), 9747–9756. doi: 10.1029/JC088iC14p09747

Raubenheimer, B., Elgar, S., & Guza, R. T. (1998). Estimating wave heights from pressure measured in sand bed. *Journal of Waterway, Port, Coastal and Ocean Engineering*, *124*(3), 151–154. doi: 10.1061/(ASCE)0733-950X(1998)124:

3(151)
Senet, C. M., Seemann, J., Flampouris, S., & Ziemer, F. (2008, aug). Determination of bathymetric and current maps by the method DiSC based on the analysis of nautical X-band radar image sequences of the sea surface (November 2007). *IEEE Transactions on Geoscience and Remote Sensing*, *46*(8), 2267–2279. doi: 10.1109/TGRS.2008.916474
Senet, C. M., Seemann, J., & Ziemer, F. (2001, mar). The near-surface current velocity determined from image sequences of the sea surface. *IEEE Transactions on Geoscience and Remote Sensing*, *39*(3), 492–505. Retrieved from `http://ieeexplore.ieee.org/document/911108/` doi: 10.1109/36.911108
Streßer, M., & Horstmann, J. (2019, mar). Remote Quantification of Nearshore Wave Energy Dissipation Rates from Coherent X-Band Radar Backscatter. In *2019 ieee/oes twelfth current, waves and turbulence measurement (cwtm)* (pp. 1–6). IEEE. Retrieved from `https://ieeexplore.ieee.org/document/8955284/` doi: 10.1109/CWTM43797.2019.8955284
Streßer, M., Seemann, J., Carrasco, R., Cysewski, M., Horstmann, J., Baschek, B., & Deane, G. (2021). On the Interpretation of Coherent Marine Radar Backscatter From Surf Zone Waves. *IEEE Transactions on Geoscience and Remote Sensing*. Retrieved from `https://ieeexplore.ieee.org/document/9518366/` doi: 10.1109/TGRS.2021.3103417
Svendsen, I. A. (1984, nov). Wave heights and set-up in a surf zone. *Coastal Engineering*, *8*(4), 303–329. Retrieved from `https://linkinghub.elsevier.com/retrieve/pii/0378383984900280` doi: 10.1016/0378-3839(84)90028-0
Svendsen, I. A. (2005). *Introduction to Nearshore Hydrodynamics* (Vol. 24). WORLD SCIENTIFIC. Retrieved from `https://www.worldscientific.com/worldscibooks/10.1142/5740` doi: 10.1142/5740
Valenzuela, G. R. (1978). Theories for the interaction of electromagnetic and oceanic waves - A review. *Boundary-Layer Meteorology*, *13*(1-4), 61–85. doi: 10.1007/BF00913863